BBA - Bioenergetics 1863 (2022) 148596

Contents lists available at ScienceDirect

BBA - Bioenergetics

journal homepage: www.elsevier.com/locate/bbabio

Small angle neutron scattering and lipidomic analysis of a native, trimeric PSI-SMALP from a thermophilic cyanobacteria☆

Nathan G. Brady [a,1], Shuo Qian [b,c], Jon Nguyen [a,2], Hugh M. O'Neill [b], Barry D. Bruce [a,d,e,*]

[a] Department of Biochemistry & Cellular and Molecular Biology, University of Tennessee, Knoxville, TN 37996, USA
[b] Neutron Scattering Division, Oak Ridge National Laboratory, Oak Ridge, TN 37831, USA
[c] The Second Target Station Project, Oak Ridge National Laboratory, Oak Ridge, TN 37831, USA
[d] Department of Chemical and Biomolecular Engineering, University of Tennessee, Knoxville, TN 37996, USA
[e] Department of Microbiology, University of Tennessee, Knoxville, TN 37996, USA

ARTICLE INFO

Keywords:
Photosystem I (PSI)
Styrene maleic acid lipid particle (SMALP)
Small angle neutron scattering (SANS)
Lipidomics

ABSTRACT

The use of styrene-maleic acid copolymers (SMAs) to produce membrane protein-containing nanodiscs without the initial detergent isolation has gained significant interest over the last decade. We have previously shown that a Photosystem I SMALP from the thermophilic cyanobacterium, *Thermosynechococcus elongatus* (PSI-SMALP), has much more rapid energy transfer and charge separation in vitro than detergent isolated PSI complexes. In this study, we have utilized small-angle neutron scattering (SANS) to better understand the geometry of these SMALPs. These techniques allow us to investigate the size and shape of these particles in their fully solvated state. Further, the particle's proteolipid core and detergent shell or copolymer belt can be interrogated separately using contrast variation, a capability unique to SANS. Here we report the dimensions of the *Thermosynechococcus elongatus* PSI-SMALP containing a PSI trimer. At ~1.5 MDa, PSI-SMALP is the largest SMALP to be isolated; our lipidomic analysis indicates it contains ~1300 lipids/per trimeric particle, >40-fold more than the PSI-DDM particle and > 100 fold more than identified in the 1JB0 crystal structure. Interestingly, the lipid composition to the PSI trimer in the PSI-SMALP differs significantly from bulk thylakoid composition, being enriched ~50 % in the anionic sulfolipid, SQDG. Finally, utilizing the contrast match point for the SMA 1440 copolymer, we also can observe the ~1 nm SMA copolymer belt surrounding this SMALP for the first time, consistent with most models of SMA organization.

1. Introduction

Oxygenic photosynthesis is the process by which plants, algae and cyanobacteria convert sunlight into chemical energy, fueling all life on earth. The initial capture of photonic energy and conversion to electrical energy, termed the light reactions, occur in galactolipid rich membranes

Abbreviations: DCPIP, 2,6-Dichlorophenolindophenol; BCA, Bicinchoninic acid protein analysis; chl, Chlorophyll; CMP, Contrast match point; D_2O, Deuterium oxide; DGDG, Digalactosyldiacylglycerol; HFIR, High Flux Isotope Reactor; KLRC, Kansas Lipidomics Research Center; LH2, Light harvesting 2 complex; D_{MAX}, Maximum particle diameter; MGDG, Monogalactosyldiacylglycerol; ORNL, Oak Ridge National Laboratory; P(R), Pairwise distance distribution analysis; PG, Phosphatidylglycerol; PSI, Photosystem I; PSII, Photosystem II; R_g, Radius of gyration; Q, Scattering angle; I, Scattering intensity; SANS, Small angle neutron scattering; SAXS, Small angle X-ray scattering; SDS-PAGE, Sodium dodecyl sulfate−polyacrylamide gel electrophoresis; SD, Standard deviation; SMA, Styrene maleic acid; SMALP, Styrene maleic acid lipid particle; SQDG, Sulfoquinovosyldiacylglycerol; Te, *Thermosynechococcus elongatus*.

☆ This manuscript has been authored by UT-Battelle, LLC under Contract No. DE-AC05-00OR22725 with the U.S. Department of Energy. The United States Government retains and the publisher, by accepting the article for publication, acknowledges that the United States Government retains a non-exclusive, paid-up, irrevocable, worldwide license to publish or reproduce the published form of this manuscript, or allow others to do so, for United States Government purposes. The Department of Energy will provide public access to these results of federally sponsored research in accordance with the DOE Public Access Plan (http://energy.gov/downloads/doe-public-access-plan).

* Corresponding author at: Department of Biochemistry & Cellular and Molecular Biology, University of Tennessee, Knoxville, TN 37996, USA.
E-mail address: bbruce@utk.edu (B.D. Bruce).
[1] **NGB Current Address:** Center for Integrated Nanotechnologies, Sandia National Laboratories, Albuquerque, NM, 87185, USA.
[2] **JN Current Address:** School of Molecular Sciences, Arizona State University, Tempe, Arizona, 85,287, USA.

https://doi.org/10.1016/j.bbabio.2022.148596
Received 7 November 2021; Received in revised form 5 June 2022; Accepted 11 July 2022
Available online 16 July 2022
0005-2728/© 2022 Elsevier B.V. All rights reserved.

called thylakoids. In plants and algae, these membranes reside within an organelle called the chloroplast, resulting from the endocytosis of a cyanobacteria. In other words, cyanobacteria are the ancestors of the chloroplast. Over the course of this evolution, the architecture of the thylakoid membranes and the proteins embedded within them have changed to suit the needs of the organism, as life proceeded onto land.

Across these kingdoms, oxygenic photosynthesis occurs in concert among variants of the following four protein complexes: photosystem II (PSII), cytochrome b_6f, photosystem I (PSI), and ATP synthase. From cyanobacteria to plants, these protein complexes have remained relatively unchanged considering oligomeric states of their individual domains, with the exception of PSI. PSI exists as a trimer in cyanobacteria [1], displaying 3-fold radial symmetry, and as a monomer in plants and algae. Recently, PSI has been shown to exist as a tetramer in heterocyst forming cyanobacteria, which has been proposed to be an intermediate state in the monomerization of PSI [2]. This dynamic evolutionary history has led to speculation as to how these structural differences affect the overall function or activity of PSI in vivo, and further, how various extraction methods may alter this activity in vitro through modification of the thylakoid lipid environment [3].

Within the trimeric PSI complex from *Thermosynechococcus elongatus* (Te), each monomer is ellipsoidal in shape, with near 2-fold symmetry between the core protein subunits PsaA and PsaB [4]. These core subunits each contain 11 transmembrane helices, and bind nearly all of the 96 chlorophyll molecules responsible for funneling light energy to the reaction center, where charge separation occurs [5]. This complex is comprised of 12 protein subunits, PsaA, B, F, I, J, K, L, M, and X contributing to a total of 32 transmembrane helices, with PsaC, D, and E being bound to the stromal surface in the middle of the monomeric ellipsoid, toward the center of the trimer [5,6]. The latter 3 subunits are often referred to as "the stromal hump" and protrudes ~30 Å into the stroma, whereas the converse (lumenal) face is relatively flat, with a ~ 30 Å indentation in the center [6]. This indentation occurs within the region of the reaction center, possibly to facilitate reduction of the reaction center by the soluble electron carrier cytochrome c_6, following a photooxidation event. In a seminal cryo-EM study from 1994, Boekema et al. show that upon dissociation of cyanobacterial PSI trimers into monomers using detergents, the outer contour of cyanobacterial PSI monomers differs greatly depending on the solubilization conditions. The authors posit that these structural changes are caused by differing lipid:detergent ratios in the proximal environment of the monomers [6]. Seven years later, Jordan et al. report 4 lipid molecules in the crystal structure of trimeric PSI from Te, near the core of the PSI complex. This coupled with the binding of an antennae chlorophyll molecule by one of these lipids, suggest that these lipids are not merely artifacts arising from sample preparation, but are integral and important to the function of the PSI complex [5].

Cyanobacterial thylakoid membranes are primarily composed of the following four lipids: monogalactosyldiacylglycerol (MGDG), digalactosyldiacylglycerol (DGDG), sulfoquinovosyldiacylglycerol (SQDG), and phosphatidylglycerol (PG), at ~45 %, 25 %, 15–25 %, and 5–15 %, respectively [7,8]. The predominant lipid in these membranes, MGDG, is unusual in that it is an example of a H_{II}-phase forming lipid, in part due to the high degree of unsaturation within the acyl chains. MGDG is a very prevalent polar lipid in all phototrophs and has been described as the most abundant polar lipid in nature [9]. The interaction of membrane proteins and lipids can be highly specific and have been shown to be critical in the overall function and structural integrity of bioenergetic protein complexes, such as PSI and PSII, as well as ion channels and receptors [10].

In PSII from Te, anionic lipids PG and SQDG are found only in pockets containing positively charged residues, mainly Lys and Arg, whereas negatively charged Glu and Asp bind MGDG and DGDG. These bound lipids are present at the interface of the dimeric PSII complex, a dynamic interface that is required to associate and dissociate rapidly to allow for the exchange of individual core subunits. Additionally, nearly 1/3 of the chlorophyll molecules in Te PSII are coordinated at their chlorin ring by a lipid molecule [8]. This coordination of pigment molecules by lipids is also reported in the light harvesting 2 complex (LH2) of *Rhodobacter sphaeroides*. Upon insertion into lipid nanodiscs, the rate of energy transfer between two highly coordinated bands of bacteriochlorophyll increased 30 %. The authors suggest that the lipids serve to orient the pigment molecules for optimal energy transfer [11]. The nanodiscs used in this study are comprised of synthetic lipids meant to mimic the target membrane and are bound by membrane scaffolding proteins, such as originally described by Bayburt et al. in 2002 [12]. While this approach does demonstrate the importance of lipids on the function of membrane proteins, it still requires the protein to be initially solubilized in detergent prior to reconstitution and insertion into the nanodiscs. In light of these drawbacks, a new technique utilizing amphiphilic copolymers, such as styrene maleic acid (SMA), have gained considerable interest over the last decade as an alternative to detergent solubilization. This process yields protein nanodiscs while retaining the native lipid environment surrounding and throughout membrane protein complexes, preserving more native function in solution [13]. These particles are referred to as SMA lipid particles, or SMALPs, and for comprehensive reviews into the current capabilities in this burgeoning field, please refer to Overduin and Esmaili, 2019 [14], and Unger et al., 2021 [15]. We have previously shown that SMA 1440 from Cray Valley (now part of Polyscope) is most efficient in solubilizing thylakoid membranes from Te [3]. Though the vast majority of SMALP studies use copolymers that are 2:1 or 3:1 [16], the styrene to maleic acid ratio (S:MA) of SMA 1440 is reported as 1.5:1. However, we previously determined the ratio to be closer to 1.21:1 by NMR [17], and approximately 37.5 % of the carboxylates in SMA 1440 have been esterified with butoxyethanol (Fig. 1), further increasing its hydrophobicity and potentially allowing for favorable interaction with galactolipid rich

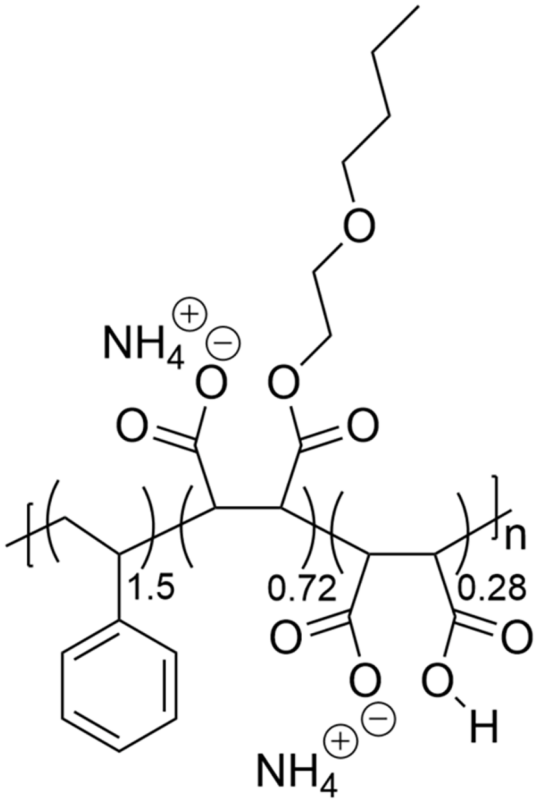

Fig. 1. Structure of SMA 1440 copolymer used in this work. The ratio of styrene to maleic acid groups is 1.5 and 72 % of the maleic acid groups have been functionalized with butoxy-ethanol following hydrolysis with ammonium hydroxide.

membranes, by mechanisms yet to be fully understood [3].

Here, we report the dimensions of trimeric PSI from Te, the largest SMALP to be reported to date, determined by small angle neutron scattering (SANS) techniques. The ability to examine protein structure at room temperature using SANS allows for an ensemble measurement to be conducted across the natural dynamics of soft matter at physiological temperatures, potentially giving a more accurate sense of protein overall particle dimensions, as opposed to movement constraints caused cryogenic temperatures in typical EM studies [18]. Previously, small-angle X-ray scattering (SAXS) of SMA particles free in solution, in the absence of lipid or protein, suggest that SMA copolymers form prolate ellipsoidal (egg shaped) particles, with SMA 1440 particles 80–100 Å in maximum diameter, ~40–60 % larger than non-esterified SMA formulations [19]. The addition of this ester group has been shown to increase the rate of SMA 1440 partitioning to the air-water interface, compared to the same backbone copolymer without the ester group [20]. Recent neutron reflectivity studies suggest that galactolipid rich monolayers allow for deep insertion of styrene and butoxyethanol portions of SMA 1440 into the hydrophobic tail region of the lipids [20]. Once formed, PSI-SMALP from Te have demonstrated a 3 nm red-shift in chlorophyll fluorescence, suggesting a more native orientation of the chlorophyll antennae within the PSI, as well as faster reduction kinetics following a photooxidation event [3]. The latter observation may be related to an ultra-fast charge separation event that has been observed within PSI-SMALP by transient absorption femtosecond spectroscopy. This study shows a 1000 fold increase in the charge separation event of PSI-SMALP (~80 fs) over detergent solubilized complex (36 ps) [21]. Using the powerful tools of contrast variation and matching available only to SANS, we present here a detailed dimensional analysis of the ~1.47 MDa PSI-SMALP [3], breaking it into its individual components of protein core, lipid annulus and copolymer or detergent micelle layers (for PSI-DDM control).

Contrast variation in SANS experiments is achieved through exploitation of the large variation in scattering length density between the hydrogen atom and its heavy isotope deuterium. By varying the amount of D_2O in the solvent, one can take advantage of contrast match points, which correspond to the fraction of D_2O in the solvent at which various system components (i.e. protein, lipid, polymer or detergent) effectively become "invisible" to the neutron beam [22–24]. Utilizing this approach, along with supporting analyses including NMR and cryoEM, Jamshad et al. demonstrated in 2015 that in SMALPs without protein, the styrene moiety interacts directly with the acyl chains of the lipids and the SMA forms a belt ~9 Å in thickness around the particle [25]. Similarly, following determination of the contrast match point of SMA 1440 at ~27 % D_2O, we report here a SMA polymer belt around PSI-SMALP ~10 Å in thickness, wrapping a discoidal particle ~354 Å in diameter. Using the previously determined contrast match point of DDM at 18 % D_2O, we determine PSI-SMALP is ~30 % larger than PSI-DDM [26,27]. We also discovered the ability of Te to survive growth in up to at least 70 % D_2O, allowing for in vivo labeling of lipids and PSI trimer, significantly lowering incoherent scattering in SANS analyses and afford opportunities to exploit contrast variation to study different component selectively (Fig. 2).

2. Materials and methods

2.1. Growth conditions and in vivo D_2O labeling of Thermosynechococcus elongatus

Te was cultured in BG-11 medium at 45 °C in an airlift bioreactor. The flat panel bioreactor (Photon Systems Instruments) was illuminated with 50 μmol photons m^{-1} s^{-1} of both red (~680 nm) and full spectrum white LEDs. Cells were harvested at OD ranging from 0.8 to 1.2 in late log phase. The cells were pelleted at 10,000 x g and stored at −80 °C prior to thylakoid membrane isolation. To improve contrast for SANS experiments, *Te* was also grown in deuterated BG-11 medium with up to

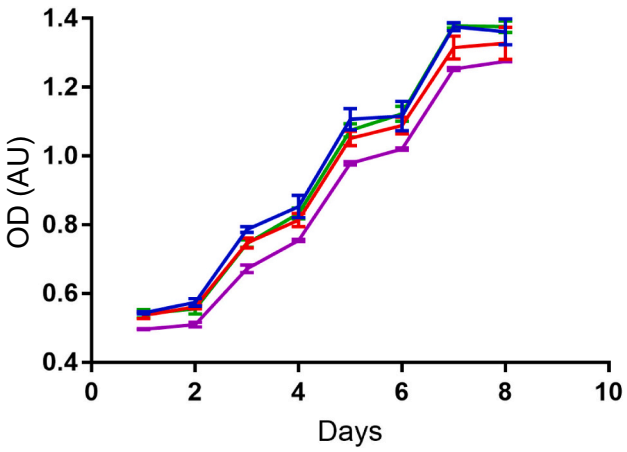

Fig. 2. Growth Curve of Te in D_2O. OD corresponds to absorbance measurements made at 680 nm. Percentages of D_2O in the BG-11 medium are as follows: 0 % (blue), 50 % (red), 60 % (green), and 70 % (purple). PSI grown in BG-11 containing 70 % D2O was used for this study.

in 2 L bottle cultures. In this case, the *Te* cells were acclimated to increasing levels of deuterium oxide in the BG-11 medium, up to a maximum 70 % (*v*/v) D_2O.

2.2. Isolation of thylakoid membranes

Thylakoid membranes were isolated from *Te* as previously described [3]. Briefly, cells being prepared for detergent solubilization with DDM were brought up in Buffer D (50 mM MES-NaOH, pH = 6.5, 5 mM $CaCl_2$, 10 mM $MgCl_2$). Cells being prepared for solubilization with SMA copolymer were brought up in Buffer S (50 mM Tris-HCl, pH = 9.5, 125 mM KCl). Chlorophyll concentration was determined using established protocols [28]. Cells were diluted to 1 mg/mL chlorophyll in their respective buffers plus 500 mM sorbitol for cell lysis. The cells were lysed 3 times using a French press at 1.8×10^8 Pa. The lysate was then spun at 10,000 x*g* for 10 min to pellet unbroken cells. The thylakoid membrane rich supernatant was then pelleted following a spin at 180,000 x g for 30 min. These thylakoid membrane pellets were then washed by resuspension in their respective buffers and Dounce ground glass homogenization 3 times prior to solubilization.

Solubilization of PSI complexes with DDM detergent and SMA copolymer.

Washed thylakoid membranes, at a concentration of 1.0 mg/mL chlorophyll, were solubilized with DDM and SMA in their respective buffers. For detergent solubilization, 0.6 % (*w*/*v*) was added to the thylakoid membrane suspension and incubated at 25 °C in a circulating water bath for 1 h. The SMA solubilization was carried out with 1.7 % (w/v) SMA copolymer and incubated at 40 °C for 3 h, with gentle agitation (250 rpm on an orbital shaker table).

2.3. SDS-PAGE

Sodium dodecyl sulfate−polyacrylamide gel electrophoresis (SDS–PAGE) analysis was performed using a sample solubilization buffer containing 350 mM dithiothreitol and 4 % SDS. The samples were heated in a 65 °C water bath for 9 min prior to loading onto a 4–20 % Bio-Rad pre-cast gel and then stained with CBB. The gel was then imaged using a Bio-Rad ChemiDoc MP gel imaging system. The MW standards used were Bio-Rad Precision Plus Protein Unstained Standards.

2.4. Small angle neutron scattering

The SANS experiment was performed at the Bio-SANS instrument at the High Flux Isotope Reactor (HFIR) of Oak Ridge National Laboratory

[29]. A single instrument configuration with the small-angle detector at 15.5 m and the wide-angle detector at 1.3 m to the sample was used to collect the data within the scattering vector Q range needed. $Q = 4\pi\sin\theta/\lambda$, where 2θ is the scattering angle, λ is the wavelength, set to 6 Å with the wavelength spread $\Delta\lambda/\lambda = 15$ %. All samples were measured in round quartz cells (Hellma USA, Plainview, NY) with a path length of 1 mm on a temperature-controlled sample holder. The SANS data were corrected for instrument dark current, detector sensitivity, detector geometry, incident beam normalization, sample transmission, and solvent background by using the facility supplied data reduction software Mantid. The resulting curves were then inspected using PRIMUS software, within which the radius of gyration (R_g) and maximum particle diameter (D_{MAX}) were then determined using the inverse Fourier transform method, carried out in GNOM [30,31].

To determine the contrast match point (CMP) of SMA 1440, equal amounts of the copolymer were analyzed by SANS at ratios of 24 %, 33 %, 43 %, 58 %, and 70 % D_2O (*v*/v) in the sample buffer. The CMP of SMA 1440 was found by plotting the square root of the intensity over the fraction of D_2O in the buffer. The X-intercept of the linear regression analysis, which corresponds to the CMP, comes out to 26.6 % (Fig. 3). The samples were subjected to the beam for ~3 h each. Following data averaging and background subtraction, the quality of the SANS data can be assessed by plotting the scattering intensity (I) against scattering angle (Q) in a double logarithmic scale (Figs. 4A and B). Solution scattering techniques, such as SANS and SAXS, require the particles to be monodisperse. The R_g can be determined from the slope of the linear regression, as previously discussed in the literature [30,31].

2.5. Laser flash photolysis

The samples for flash photolysis were measured at 10, 30, and 90 μg/mL Chl a using a Joliot-type spectrophotometer (JTS-100) [32]. Total Chl a extractions were performed on PSI-DDM and PSI-SMALP with 90 % methanol (as previously described) [28]. At time equal to zero, all P700 in the sample is oxidized by a bright actinic flash and the Abs_{810} results from the production of $P700^+$. This photooxidized species is then rapidly reduced back to P700 by 2,6-Dichlorophenolindophenol (DCPIP). Upon photoexcitation, PSI becomes oxidized and the absorbance of 830 nm light disappears. As PSI becomes reduced, the absorbance signal of 830 nm returns. The rate at which this occurs can be plotted and rate constants can be determined. Reduction kinetics of P700 reaction center within PSI by various ratios of native cytochrome c_6 soluble electron carrier and bovine cytochrome were measured for PSI-DDM and PSI-SMALP. Observed reduction rate constants (K_{obs}) are plotted along with residuals, and the associated rate constants were calculated. Fitting was done with a single exponential decay in Prism 9.

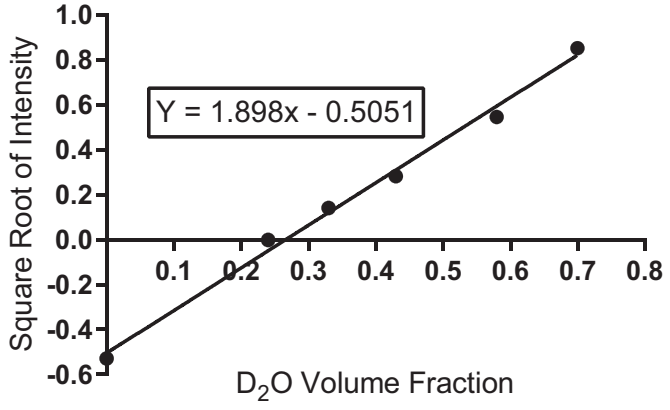

Fig. 3. Small angle neutron scattering intensity of SMA 1440 at various D_2O volume fractions. The Y-intercept corresponds to the contrast match point of SMA 1440.

2.6. Tandem mass spectrometry lipidomics

Mass spectrometry on a Xevo TQ-S (Waters Co., Milford, MA) was used to analyze the intact lipids by direct infusion with precursor and neutral loss scans, using the scans shown in Table S1. Data were processed as described by Xiao et al. (2010) [33]. Except as noted for SQDG, internal standards were detected by the same scan as the analytes. Response factors were applied to the MGDG and DGDG analyses to correct for differences in the response of the mass spectrometer to unsaturated galactolipid species compared to the saturated internal standards. In addition, because the samples contained molecular species that were the same as the internal standards, the samples were analyzed with and without the internal standards, and ratios among peak intensities in the two analyses were used to correct the internal standard intensities and calculate the amounts of the naturally occurring lipids that matched the internal standards.

3. Results and discussion

Initially, we used SANS with contrast variation to determine the contrast match point (CMP) of SMA 1440 at ~27 % D_2O as described in the Materials and Methods. The CMP for DDM has been identified previously by a similar approach to be 18 % D_2O [27]. SANS measurements of PSI-SMALP and PSI-DDM were then performed in full contrast and at CMP conditions for DDM and SMA 1440 (Fig. 4A, B). The monodispersity of our samples are confirmed by Guinier analysis, where a linear response is shown in the Guinier region, which is defined as the portion of the scattering curve at which $QR_g < 1.3$ when the scattering data is plotted as Ln(I(Q)) versus Q^2 (Figs. 4C and D) [30,31].

The radii of gyration for PSI-DDM and PSI-SMALP at full contrast and at the respective CMPs for DDM and SMA 1440 are shown below in Table 1. From the linearity of the Guinier fit, we ruled out the possibility of coexistence of different oligomers such as dimer and trimer. For the purposes of this investigation, the core represents the PSI trimer and any retained thylakoid lipids, and the shell represents the contribution of the DDM toroid or SMA copolymer belt surrounding the particle, to the neutron scattering profile. To achieve full contrast, protiated PSI (hPSI) was measured in 100 % D_2O in the case of PSI-DDM, and reciprocally, deuterated PSI (dPSI) was measured in 100 % H_2O for PSI-SMALP. Isotopic effects between dPSI and hPSI were minimal, as demonstrated by the comparable R_g values for hPSI-DDM and dPSI-DDM at 18 % D_2O (Table 1). Further, the R_g values for PSI-DDM agree with previously published results, which report 77.9 and 94.9 Å for PSI-DDM at 18 and 100 % D_2O, respectively [27]. Therefore, outside of Table 1 and the Fig. 4 legend, these samples will be referred to as simply "PSI-DDM" and "PSI-SMALP," for clarity.

In similar fashion, we next performed a pairwise distance distribution analysis (also referred to as P(R) analysis) to obtain D_{MAX} for PSI-DDM and PSI-SMALP at their respective CMP and full contrast (Figs. 4E & F). The slightly asymmetrical shape and of these curves suggests an elongated shape, such as a oblate ellipsoid (egg shaped) or discoidal in geometry as we would expect, with PSI-SMALP displaying more exaggerated features in this region at high R (Fig. 4F) [19]. The maximum dimension (D_{MAX}) of these P(R) curves is another approach to estimate the overall particle size and as we would expect, they shift to higher R in full contrast than in DDM or SMA-contrast matched condition. The x-intercept at high R corresponds to the D_{MAX} of PSI-DDM (Fig. 4E) and PSI-SMALP (Fig. 4F). The results are highly consistent with our recent results with TEM imaging of PSI-SMALPS which observed a larger particle diameter for the PSI-SMALP particles (34.7 nm) than the PSI-DDM particles (21.5 nm) [17].

Using D_{MAX} of these particles at full contrast and at their corresponding CMPs, we can build a detailed model depicting the dimensions of PSI-DDM and PSI-SMALP (Fig. 5). These data support previous findings that SMA forms a tight belt, ~10 Å in thickness with very little protrusion from the particle. Conversely, the difference in D_{MAX} between

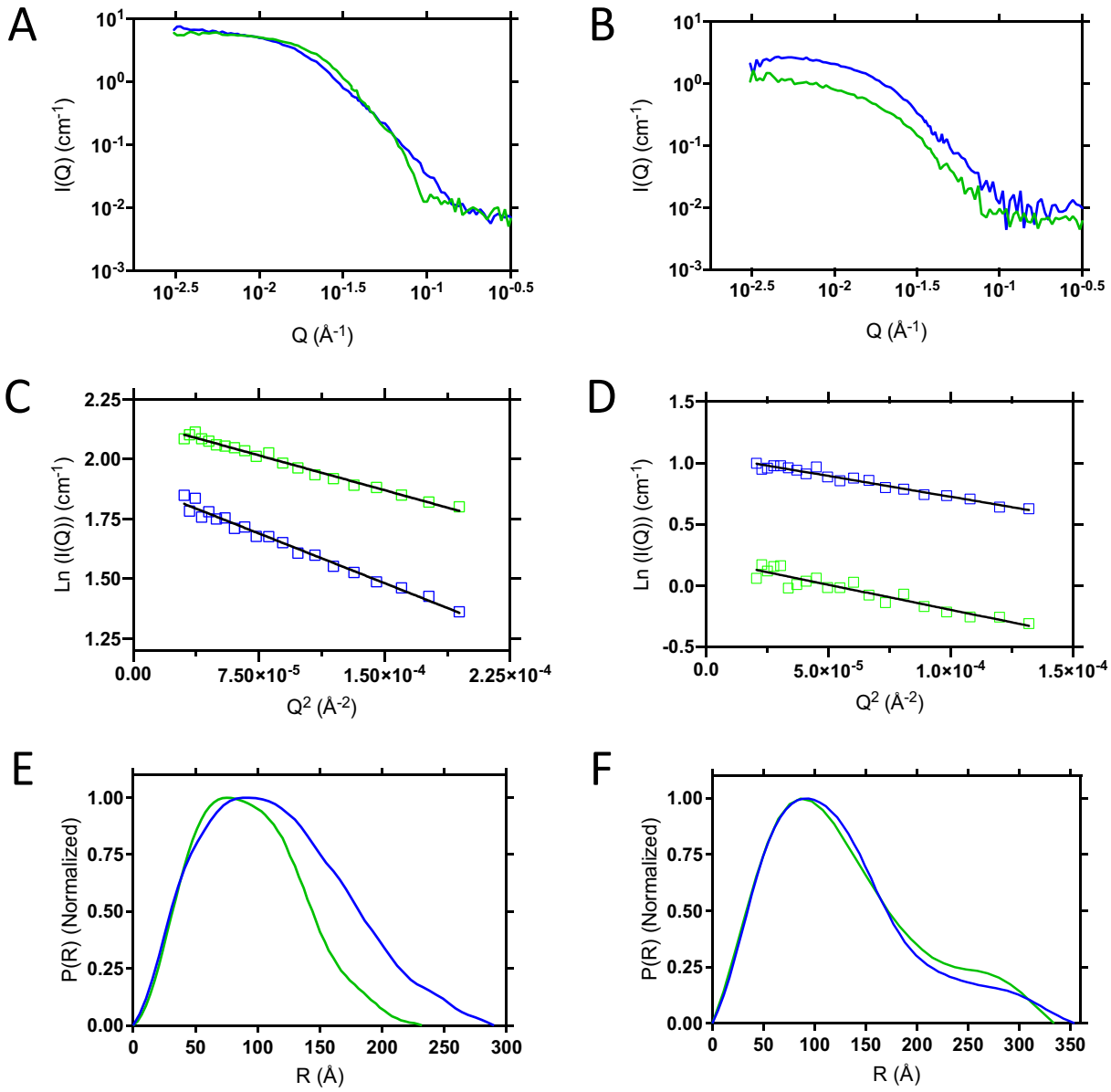

Fig. 4. SANS analyses of PSI-DDM (A, C, and E) and PSI-SMALP (B, D, and F). (A) SANS curves of dPSI-DDM at 18 % D2O (green) and hPSI-DDM at 100 % D2O (blue), (B) SANS curves of dPSI-SMALP at 27 % D2O (green) and dPSI-SMALP at 100 % H2O (blue). (C) Guinier analysis of hPSI-DDM at 100 % D2O (blue) and dPSI-DDM at 18 % D2O (green). (D) hPSI-SMALP at 100 % D2O (blue) and dPSI-SMALP at 27 % D2O (green). For C and D, linear trend lines (black) are superimposed over square data points. (E) Pairwise distance distribution analysis of dPSI-DDM at 18 % D2O (green) and hPSI-DDM at 100 % D2O (blue), and (F) dPSI-SMALP at 27 % D2O (green) and dPSI-SMALP at 100 % H2O (blue).

Table 1
Radii of gyration for PSI-DDM and PSI-SMALP by SANS at respective CMPs and at full contrast.

Protein condition	Percent D_2O (v/v)	R_g (error, Å)	QR_g (limit < 1.3)	Comments
hPSI-DDM	100	90.04 (0.91)	1.26	Overall structure of purified PSI + DDM
hPSI-DDM	18	73.49 (3.87)	1.25	PSI only, DDM is contrast matched
dPSI-DDM*	18	72.37 (0.86)	1.06	PSI only, DDM is contrast matched
dPSI-SMALP	0	101.9 (4.44)	1.06	PSI + lipids + SMA copolymer belt
dPSI-SMALP*	27	112.36 (4.38)	1.23	PSI + lipids only, SMA is contrast matched

* dPSI at contrast match point of shell provides improved contrast between protein and buffer.

PSI-DDM measured at full contrast and 18 % CMP_{DDM} is much more significant, at 29 Å. This is reasonable when you consider the architecture of the toroid (Fig. 5, inset), where the detergent layer will extend the full length of the DDM detergent molecule. At the same time, the particles in PSI-SMALP are significantly larger than PSI-DDM, regardless the contrast conditions measured. The increased size of PSI-SMALP is shown here to be due to retained native lipids, as is widely reported in the literature to be the case with SMALPs [3,34–36]. Indeed, we confirm this to be the case with trimeric PSI from Te as well by tandem mass spectrometry. The subunit profiles of PSI-DDM and PSI-SMALP used in these lipidomics experiments are similar to previous reports [3] and confirm the presence of all major subunits for both sample preparations (Fig. 6). All four thylakoid lipids are enriched in PSI-SMALP, with fold increases of 20 for DGDG, 37 for MGDG, 18 for PG and 60 for SQDG compared to PSI-DDM (Table 2). These lipid species are reported as nanomoles lipid per mg PSI protein and the standard deviation (SD) for

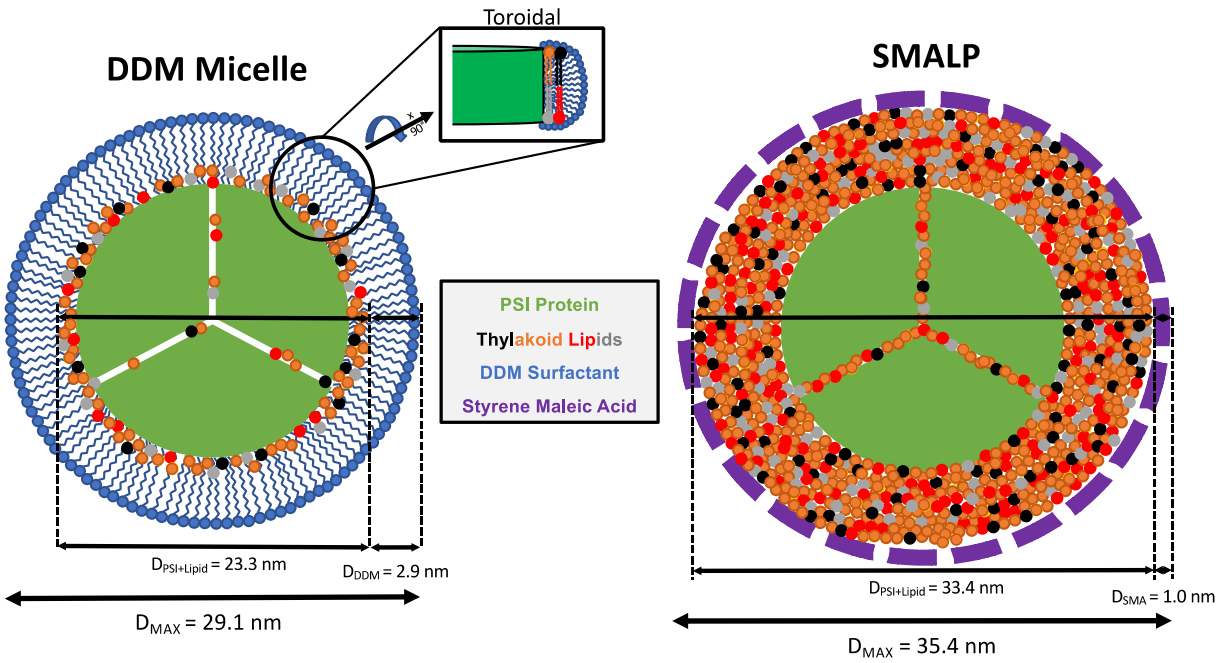

Fig. 5. Model of PSI-DDM and PSI-SMALP. Note: lipids are not identified or quantified in this cartoon.

each data point were calculated across three biological triplicate samples. The SD for each lipid class (i.e. DGDG, MGDG, etc.), as well as total lipid values for SMALP and DDM preparations, were calculated using Eq. 1.

$$Total\ SD = \sqrt{\left(SD_1{}^2 + SD_2{}^2 + \ldots \right)} \quad (1)$$

As part of SANS data analysis, we attempted to reconstruct the low-resolution model using ab initio methods such as DAMMIF or DAMMIN in the ATSAS package. However, the large discoidal shape is known to pose a challenge for these methods, and no sensible structures were obtained. All data listed in Table 1, however, can be fit well with simple elliptical cylinder and discoidal models (Figs. S1 and S2) without accounting for the inhomogeneity in scattering density within a particle, e.g., between protein and lipids (Tables S2 and S3). With less structural parameters involved in these simple models, the results provide a robust approximation on the overall shape only. From these results, the particles (regardless of being isolated within DDM or SMALP) show a thickness of about 4-7 nm. This range arises from the inherent ambiguity of using simple models to describe highly dynamic structures. The only driving force for fitting here is the chi-square, which has nothing to do with the physical reality. Future investigations using a physically constrained MD simulation model may yield more precision in determining this *Z*-dimension. However, with these simple models offering less bias to the structural results, we can see PSI-DDM fits very well in the discoidal and elliptical models due to its more static nature in the X- and Y-dimensions, having been stripped of its native membrane environment. Conversely, the PSI-SMALP shows a larger disparity in its fits due to the dynamic nature of the lipid annulus. This observation is also supported by the P(R) analysis, as the symmetric curves for PSI-DDM suggest a more symmetric particle shape (Fig. 4E) and the curves for PSI-SMALP are much more extended, presumably suggesting a more extended membrane sheet, which by its nature would be undulating (Fig. 4F). R_g as the radius of gyration is a good indicator of size for globular particles. However, because we are looking at very extended, discoidal structures that are highly dynamic in solution, P(R) is a much stronger indicator of size and shape in this case. For this reason, we only discuss D_{MAX} as the determination of size throughout this work. Being that the two dimensions for PSI-SMALP at the CMP and at full contrast are so close, suggests that SMA belt is tightly wrapped with little protrusion from particle. How this large lipid annulus undergoes dynamic changes in solution may be complicated by the native lipid asymmetry in the thylakoid membrane that might induce some curvature stress upon SMA solubilization. In addition, the major enrichment in the anionic sulfolipid with the PSI-SMALP compared to the total absences of sulfolipid in prior DDM isolated forms of PSI [37], may also generate some electrostatic repulsions that might alter the particle dimensions in solution (Table 2). This enhanced freedom of motion suggests the SMALP provides a less rigid membrane-mimic for the embedded membrane protein, an important factor for higher protein activity.

Lipids were quantified using tandem mass spectrometry via comparison to internal standards and the protein mass was determined by bicinchoninic acid protein analysis (BCA). However, our group previously discovered that the solubilization efficiency of plant thylakoids by a number of SMA copolymers when determined by protein mass (by BCA) and pigment content (spectrophotometrically) had a similar trend but were not exact, for purposes not fully understood [38]. For this reason, we decided to confirm the ratio of chl:protein between the DDM and SMALP extracted samples using laser flash photolysis (Fig. 7).

Each PSI monomer contains approximately 112 antennae chlorophyll (chl) molecules that are mainly coordinated within core subunits PsaA and PsaB [39]. Of these 112 spectroscopically identified Chl a molecules, 96 have been placed in the crystal structure, 1JB0 [5]. This discrepancy of 18 chlorophyll molecules, which equates to a 16.1 % loss, suggests that these chlorophylls are either lost during detergent isolation, or exist within a less resolved region of the PSI protein structure and can therefore not be assigned. These Chl a absorb light and funnel that excitation energy to a uniquely modified duo of Chl a molecules referred to as the "special pair" or P700, owing from their maximum absorbance.

Upon receipt of energy from the antennae, a photooxidation event occurs, converting the photonic energy into an electron that is then fired through the interior of the protein. The oxidized $P700^+$ also absorbs 810 nm light (Abs_{810}), a signal that is lost as $P700^+$ becomes reduced. Using a technique called flash photolysis, we can determine the number of active PSI molecules in each sample, as well as the reduction rate following the photooxidation event (Fig. 7).

The reduction of $P700^+$ occurs much slower for PSI-DDM (Fig. 7A)

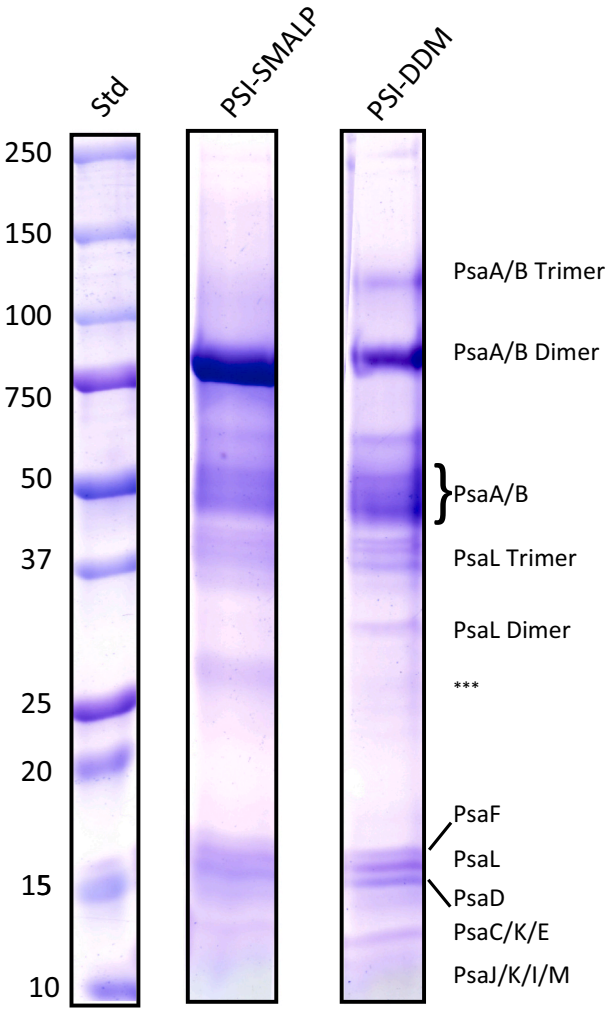

Fig. 6. SDS-PAGE showing PSI subunit profiles for PSI-SMALP and PSI-DDM. Samples were stained by CBB and the individual lanes have been combined for clarity and allow comparisons. The *** represent an unknown band(s) at ~32 kDa.

compared to PSI-SMALP (Fig. 7B), as depicted by the more gradual decay of the Abs_{810} signal over time. When analyzed with a one phase decay, a 6-fold increase in K_{obs} for PSI-SMALP reduction rate is observed over PSI-DDM (Fig. 7C). This enhanced reduction rate of PSI-SMALP by non-native electron donor horse heart cytochrome *c* has previously been shown [3]. The reason for this expedited turnover rate is not completely understood, however, ultrafast femtosecond transient absorption spectroscopy data suggests that the initial charge separation and transfer event inside PSI may occur faster within SMALP compared to DDM isolation [21]. This faster cycling of PSI-SMALP through multiple turnovers during the 100 μs actinic flash from the JTS-100 may lead to a faster final reduction of $P700^+$ on the back end of the light pulse. Across all 3 levels of Chl a tested, the [P700] in PSI-SMALP is approximately 84 % that of PSI-DDM (Fig. 7D). Being that the samples were loaded with equal total chl, these data suggest that on average 16 % of antennae Chl a is lost in DDM extraction compared to PSI-SMALP. Interestingly, this 16 % loss agrees with the discrepancies between the previously reported values of 112 and 96 Chl a molecules per PSI monomer as previously reported [5,39]. Being that both of these previous investigations used detergent solubilization, it is possible that this harsh condition destabilizes the reaction center, leading to a loss of Chl a from the antennae. Table 3 shows the concentrations of both Chl a and PSI for each of the biological triplicates (for both extraction methods) used for the lipidomics analysis in Table 2.

Table 2
Lipid totals for PSI-DDM and PSI-SMALP by tandem mass spectrometry.

Lipid (# FA carbons: # of double bonds)	PSI-DDM		PSI-SMALP	
	Lipid/protein (nmol/mg)	SD	Lipid/protein (nmol/mg)	SD
DGDG (32:0)	0.812	0.917	41.28	17.39
DGDG (32:1)	2.862	1.446	37.52	10.14
DGDG (32:2)	0.029	0.029	0.272	0.053
DGDG (33:0)	0.087	0.101	2.673	0.186
DGDG (33:1)	0.055	0.081	1.837	0.582
DGDG (34:0)	0.188	0.326	8.502	1.713
DGDG (34:1)	2.631	1.568	42.35	16.55
DGDG (34:2)	0.089	0.072	0.779	0.386
DGDG (35:0)	0.046	0.036	0.503	0.179
DGDG (36:0)	0.013	0.021	1.289	0.322
DGDG (36:1)	0.041	0.011	0.746	0.360
DGDG (36:2)	0.017	0.028	0.184	0.130
DGDG (37:1)	0.010	0.003	0.067	0.052
Total DGDG	**6.880**	**2.350**	**138.0**	**26.13**
MGDG (32:0)	0.460	0.467	25.72	13.27
MGDG (32:1)	2.856	1.268	87.33	37.25
MGDG (33:0)	ND	NA	1.306	1.190
MGDG (33:1)	0.036	0.062	3.985	1.813
MGDG (34:0)	0.547	0.736	31.77	14.17
MGDG (34:1)	2.938	1.542	105.2	46.53
MGDG (34:2)	0.045	0.020	0.814	0.347
Total MGDG	**6.883**	**2.179**	**256.1**	**62.72**
PG (32:0)	0.917	0.858	26.03	12.13
PG (32:1)	0.183	0.118	1.526	0.557
PG (34:0)	0.390	0.434	12.18	4.670
PG (34:1)	1.985	1.650	21.44	8.798
Total PG	**3.476**	**1.913**	**61.17**	**15.71**
SQDG (32:0)	4.693	4.147	340.1	153.6
SQDG (32:1)	0.174	0.109	2.598	1.124
SQDG (33:0)	0.313	0.259	21.50	7.511
SQDG (34:0)	4.779	4.444	327.7	131.1
SQDG (34:1)	2.307	1.768	41.73	17.98
SQDG (36:1)	0.012	0.013	0.530	0.405
Total SQDG	**12.28**	**6.337**	**734.1**	**202.8**
Total Lipid	**29.51**	**7.354**	**1189**	**214.5**

Using the two previously published values of 96 and 112 Chl a molecules per PSI monomer, we can calculate the presumed concentration of PSI and compare this to the PSI concentration as determined by BCA protein analysis. In both high and low Chl a cases, the determination of PSI concentration by pigment content is underestimated for DDM extracted protein. In the low Chl a case, PSI protein is highly overestimated for PSI-SMALP and assuming 112 Chl a molecules, the [PSI] concentration of PSI-SMALP is only 0.16 % lower for the pigment and BCA derived values, respectively (Table 4). Assuming the plausibility of Chl a to be lost and not added by the given extraction method, these data suggest that there are indeed 112 Chl a molecules per PSI monomer and further that ~18.5 % Chl a molecules can be lost due to detergent isolation. These data also support the protein mass as determined by BCA to scale the lipidomics results shown in Table 2. We have previously reported the partial loss of PsaF subunit following SMALP extraction [3]. The PsaF subunit is a transmembrane helix that is peripherally associated to PsaB core subunit and accounts for <5 % of the overall PSI complex by mass. Te PsaF does not contain the N-terminal extension that extends out over the solvated portion of the lumenal face of PSI in algal PSI orthologs [40]. Therefore, we speculate that the partial loss of PsaF has little effect on the binding of Cu^{2+} ions, thus conferring little change on the protein measurement by BCA and corroborate the partial loss of PsaF, though the PsaF band can still be seen at ~17 kDa (Fig. 6). Further, these data of an 18.5 % loss of Chl a for PSI-DDM agree with the 16.1 % loss of Chl a in this preparation as determined by flash photolysis (Fig. 7).

In addition to the greatly increased lipid content of PSI-SMALPs as compared to PSI-DDM, there are also distinct differences in percent

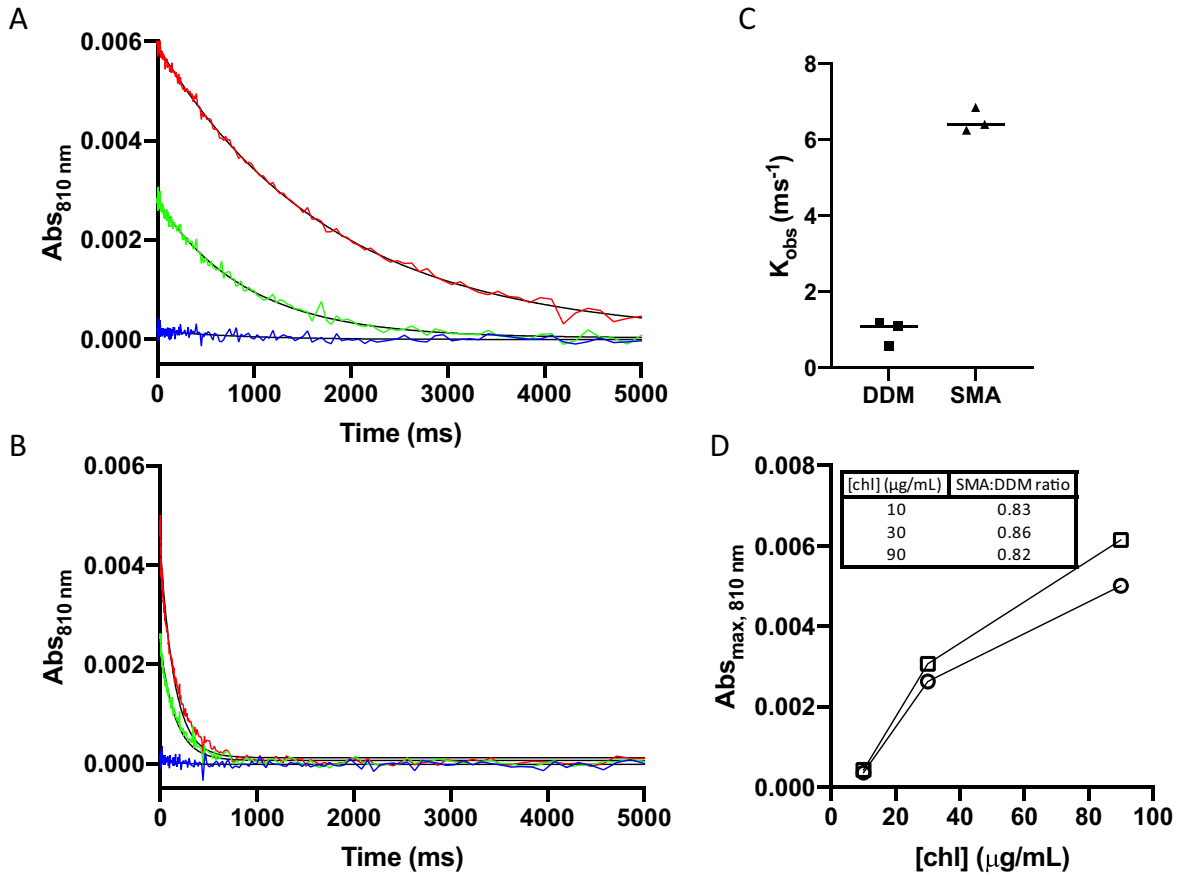

Fig. 7. Determination of P700 to antennae Chl a ratio by laser flash photolysis and turnover kinetics of PSI-DDM and SMALP by DCPIP. (A-B) Reduction of $P700^+$ by 10 µM DCPIP in (A) PSI-DDM and (B) PSI-SMALP, at 10 (blue), 30 (green), and 90 (red) µg/mL chl. (C) Observed $P700^+$ reduction rate of PSI in DDM and SMALP. (D) Maximum absorbance at 830 nm following photooxidation of PSI-DDM and PSI-SMALP at vaed [chl].

Table 3
Pigment and protein concentrations for biological triplicates used in lipidomics analysis.

Preparation	Chlorophyll assay	BCA analysis
	[Chl] (mg/mL)	[PSI] (mg/mL)
	1.130	4.37
	1.300	5.94
DDM	1.310	6.18
	0.102	0.312
	0.058	0.174
SMALP	0.123	0.530

Table 4
Percent change between PSI concentrations as determined by Chl a and BCA analysis.

Preparation	Average [chl]	Assumed	[PSI] by Chl a	[PSI] by BCA	Percent
	(mg/mL)	# Chl a Molecules	(mg/mL)	(mg/mL)	Change
		96	5.34		−2.87
DDM	1.25	112	4.48	5.50	−18.5
		96	0.403		19.0
SMALP	0.094	112	0.338	0.338	−0.156

composition regarding degree of saturation, fatty acid length, and lipid class between the two PSI particles (Fig. 8). Across all three of these parameters, the standard errors across three replicates are greater for the DDM preparation as compared to the SMALP preparation. This is likely due to the relatively few lipids remaining in the PSI-DDM preparation, and this process of delipidation may be fairly random during detergent solubilization.

The percent composition for each lipid class was also recorded for PSI-SMALP and PSI-DDM, confirming considerable differences between the lipid profiles of both PSI particles, in a side-by-side comparison without the use of any scaling factors (Fig. 8A). Perhaps most notably, SQDG is found in far higher quantities in both PSI preparations, which is in stark contrast to the 15–25 % SQDG in the overall cyanobacterial thylakoid membrane [7,8]. This increased SQDG content seems to support recent findings that suggest that this lipid is critical to the overall function of PSI in different ways. Endo et al. report in 2016 that SQDG is required for oligomerization of the PSI complex, and the absence of this lipid causes decreased electron transfer in the phycobilisome antennae complex, as well as decreased and blue-shifted chlorophyll fluorescence (suggesting disturbed chlorophyll orientation within the protein antennae) in PSI from Te [41]. The indication that this lipid is so important to the overall function of PSI, coupled with this significantly elevated level of SQDG in PSI-SMALP suggests that the proximal membrane environment surrounding PSI is itself enriched in SQDG, which is therefore being incorporated into the SMALP. Using dimensional analysis, we can convert these lipid concentrations to number of lipid molecules per PSI monomer and trimer (Table 5). The associated standard deviation from the tandem mass spectrometry lipidomics analysis were converted in similar fashion, thus relating to a +/− number of molecules for each lipid in Table 5. Keeping this significant difference in lipid quantities between the two preparations in mind, the major finding shown in Fig. 8B is that PSI-SMALP appears to be highly enriched in saturated lipids as compared to PSI-DDM. Fatty

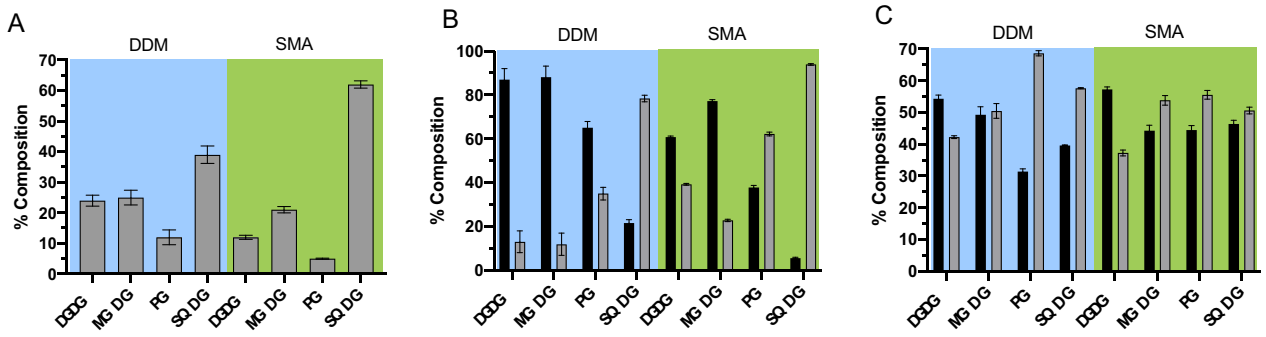

Fig. 8. Percent composition of each lipid class (A), Degree of saturation (B), and length of fatty acids (C) are shown for PSI-DDM (blue box) and PSI-SMALP (green box). (A) Overall lipid profiles by headgroup for PSI-DDM and PSI-SMALP are reported. (B) Percent of unsaturated lipids (black) and percent of saturated lipids (gray) are displayed. (C) Percent of lipids with 32 total carbon atoms (black) and 34 total carbon atoms are shown. Error bars represent standard error across three replicates.

Table 5
Number of lipid molecules for PSI monomer and trimer.

	# Lipid molecules per PSI monomer and trimer			
Lipid	DDM	SD	SMALP	SD
MGDG	2.476	1.109	92.11	31.91
DGDG	2.475	1.195	49.64	13.29
SQDG	4.416	3.223	264.1	103.2
PG	1.250	0.9732	22.00	7.991
Total (monomer)	10.62	3.740	427.8	176.1
Total (trimer)	31.85	11.22	1283	528.4

acid length seems to follow a similar trend between both preparations, with DGDG preferring two chains of 16 carbon atoms and all other lipid classes showing a preference for one chain of 16C atoms and one of 18C atoms (Fig. 8C).

To determine whether these numbers of lipid molecules agree with dimensions of PSI-SMALP as determined by SANS, we first calculated the area of the lipid annulus by subtracting the area of two circles. The first circle corresponding to the cross section of PSI as determined by D_{MAX} of PSI-DDM at the CMP for DDM (18 % D_2O, *v*/v), subtracted from the cross section of PSI-SMALP at the CMP for SMA (27 % D_2O, v/v). This approach calculates the area of the lipid annulus around PSI-SMALP is ~450 nm^2. Doubling this area to account for the lipid bilayer and using a previously determined cross sectional area for compressed cyanobacterial thylakoid lipids of 0.64 nm^2, we determine this annulus should contain ~1400 lipid molecules [42]. This value fits well within our range of 755–1812 lipids as shown in Table 5.

However, this area calculation suggests a slightly higher number of lipids molecules than the experimentally determined average, which may be due to either variations in cross-sectional lipid area or non-lipid entities being contained in the lipid annulus of PSI-SMALP, the latter will require further investigations using techniques such as proteomics, to determine.

Considering recent atomic force microscopy data, trimeric PSI in Te exists in a uniform array within the thylakoid membrane [43]. Considering the lipid profiles presented here, the gaps between the PSI complexes appear to be packed with SQDG, giving these patches of membrane unique protein and lipid identities. This enrichment of SQDG would have significant effect on the overall electrostatic landscape of these membrane domains as well, being that this lipid carries a full negative charge. Bringing these findings together lend further credibility to a hypothesis we have offered regarding the selectivity of SMA 1440 for trimeric PSI in Te thylakoids. This procedure consistently isolates trimeric PSI at ~40 % yield and does not extract PSII or any parts of the cytochrome b_6f or ATPase complexes to our knowledge [3]. This observation led to the hypothesis that if photosystems were laterally segregated in cyanobacterial thylakoids, this may cause (or result from) lateral heterogeneity in the lipid content of that membrane domain. Similar findings were recently reported supporting protein selectivity of SMA copolymers in *Synechosystis* sp. PCC6803, where the cytochrome bc_1 complex was isolated at ~70 % yield, where adjacent light harvesting proteins yielded only 10–22 % yields. Swainsbury et al. posit that this was due to the comparatively lipid rich environment of the cytochrome bc_1 complex, however the lipid profiles of each SMALP are not directly compared in this study, rendering qualitative hypotheses regarding lipid species facilitating SMA insertion/SMALP formation difficult in this case at present [44].

To test this hypothesis, we recently published a study investigating the interaction of SMA 1440 with galactolipid rich monolayers by neutron reflectometry [20]. This study found that galactolipids disrupted the packing of the monolayers, and interestingly, that the galactosyl ring coupled with the negative charge on SQDG made this lipid more disruptive to packing than DGDG, which contains two galactosyl rings and is the "bulkiest" lipid by head group volume. SMA 1440 was also found to accumulate most on SQDG containing monolayers and galactolipid containing monolayers in general allowed for deeper insertion of polymer into the monolayer [20]. These data, in light of the findings reported in this work, suggest trimeric PSI exists as a uniform array in Te, between which are membrane patches containing primarily SQDG, and that this proteo-lipid environment is most amenable to SMA 1440 insertion. Further, the functional group that sets SMA 1440 apart from other SMA formulations used for protein purification, the butoxyethanol group on nearly 1/3 of carboxylic acid moieties, may be attracted to and/or directly interact with SQDG to facilitate insertion into this region of Te thylakoids, therefore facilitating the formation of PSI-SMALP. Lastly, it should be noted that this PSI complex is derived from a thermophilic organism, however the SANS was conducted at temperatures ~30° below the physiological temperature. We cannot say with certainty how the dynamics of this system will behave at various temperatures (or those closer to physiological) at this time. We have plans to investigate this system at various temperatures and/or defined lipids to probe for differences in particle dynamics, but these experiments will take a considerable amount of time and deserve a fully fleshed out analysis unto their own.

4. Conclusions

Here we show that the thermophilic cyanobacterium Te can grow in up to 70 % deuterated media, yielding highly deuterated proteins and lipids for use in neutron scattering experiments. We also determined the contrast match point for the SMA formulation used in this study, the butoxy ethanol esterified SMA 1440, to be approximately 27 % D_2O. This finding allowed us to match out the SMA, showing a decrease in overall size of the PSI-SMALP of ~10 Å, which is in line with previous reports regarding the size of the SMA copolymer belt [25]. Similarly, the

D_{MAX} for PSI-DDM measured at the CMP for DDM and in full contrast agree with previously published results [27]. The difference in D_{MAX} between these two particles suggests an ~30 % increase in size for the PSI-SMALP compared to the detergent solubilized form. Tandem mass spectrometry corroborates that this enhanced size is due to a greater number of lipids from the thylakoid membrane retained within the SMALP. Extrapolating these lipid concentrations and normalizing for PSI concentration, we find PSI-DDM contains 31.85 ± 11.22 lipid molecules, whereas PSI-SMALP contains 1283 ± 528.4 lipid molecules per PSI trimer. Further, these data suggest that in the PSI-SMALP compared to PSI-DDM, percent composition of saturated lipids increased, the amount of 32 and 34 length carbon chains became more balanced, and the lipid class most enriched is that of the negatively charged sulfolipid; SQDG. Lastly, aside from delipidation of PSI complexes through detergent solubilization, flash photolysis spectrophotometry suggests that ~16 % of antennae chlorophyll may also be lost during this process. This loss of antennae chlorophyll seems to be mitigated through non-detergent solubilization of PSI with SMA copolymers.

Associated content

Table of mass spectrometry scan parameters and internal standards.

CRediT authorship contribution statement

NGB performed the PSI isolations, SANS data collection and analysis, lipid and protein characterizations, and manuscript writing; SQ aided in the SANS data collection, analysis and interpretation; JN maintained the cyanobacteria cultures, performed deuteration of cell culture and assisted in SANS sample dilutions; HO aided in the SANS analysis and interpretations; BDB provided conceptualization, guided work, provided funding, assisted in the SANS data collections, and contributed to figures and manuscript writing. The manuscript was written through contributions of all authors. All authors have given approval to the final version of the manuscript.

Funding sources

Support for BDB has been provided from the Gibson Family Foundation, the Dr. Donald L. Akers Faculty Enrichment Fellowship, the Charles P. Postelle Distinguished Professorship. NGB and BDB have been supported via a Joint Directed Research Development Award from University of Tennessee at Knoxville/Oak Ridge National Laboratory Science Alliance, and National Science Foundation (EPS-1004083). NGB has also been supported via a Penley Fellowship. The lipid analyses described in this work were performed at the Kansas Lipidomics Research Center (KLRC) Analytical Laboratory. Instrument acquisition and lipidomics method development were supported by the National Science Foundation (including support from the Major Research Instrumentation program; current award DBI-1726527), K-IDeA Networks of Biomedical Research Excellence (INBRE) of National Institute of Health (P20GM103418), USDA National Institute of Food and Agriculture (Hatch/Multi-State project 1013013), and Kansas State University. Bio-SANS is part of the Center for Structural Biology at Oak Ridge National Laboratory and is supported by the Office of Biological & Environmental Research (OBER) in the Department of Energy (DOE) Office of Science. This research used resources at the High Flux Isotope Reactor and Spallation Neutron Source, a U.S. Department of Energy Office of Science User Facility operated by ORNL. ORNL is operated by UT-Battelle, LLC under Contract No. DE-AC05-00OR22725 with the U.S. Department of Energy. Shuo Qian was also partly supported by the Spallation Neutron Source, Second Target Station Project, at Oak Ridge National Laboratory in this project.

Declaration of competing interest

The authors declare the following financial interests/personal relationships which may be considered as potential competing interests: Barry D. Bruce reports a relationship with North American Photosynthesis Conference Association that includes: board membership. Barry D. Bruce has patent #US Patent App. 17/594,503 pending to Inventor. Nate Brady has patent #US Patent App. 17/594,503 pending to Inventor.

Data availability

Data will be made available on request.

Acknowledgment

In memory of Prof. James (Jim) Barber, FRS: Friend, colleague, and pioneering photosynthesis investigator. We thank Ms. Alexandra Teodor for her assistance in the execution and interpretation of laser flash photolysis work (Fig. 7). The lipid analyses described in this work were performed at the Kansas Lipidomics Research Center Analytical Laboratory. We thank Jyotirmoy Mondal for help on Graphic Abstract. We also thank Professor C. Neil Hunter FRS (Department of Molecular Biology & Biotechnology, University of Sheffield, UK) for the use of his AFM image of native, un-deuterated Te thylakoid membranes in the Graphical Abstract.

Appendix A. Supplementary data

Supplementary data to this article can be found online at https://doi.org/10.1016/j.bbabio.2022.148596.

References

[1] E.J. Boekema, J.P. Dekker, M.G. van Heel, M. Rögner, W. Saenger, I. Witt, H. T. Witt, Evidence for a trimeric organization of the photosystem I complex from the thermophilic cyanobacterium Synechococcus sp, FEBS Lett. 217 (2) (1987) 283–286.
[2] M. Li, D.A. Semchonok, E.J. Boekema, B.D. Bruce, Characterization and evolution of tetrameric photosystem I from the thermophilic cyanobacterium Chroococcidiopsis sp TS-821, Plant Cell 26 (3) (2014) 1230–1245.
[3] N.G. Brady, M. Li, Y. Ma, J.C. Gumbart, B.D. Bruce, Non-detergent isolation of a cyanobacterial photosystem I using styrene maleic acid alternating copolymers, RSC Adv. 9 (54) (2019) 31781–31796.
[4] P.R. Chitnis, Photosystem I, Plant Physiol. 111 (3) (1996) 661.
[5] P. Jordan, P. Fromme, H.T. Witt, O. Klukas, W. Saenger, N. Krauß, Three-dimensional structure of cyanobacterial photosystem I at 2.5 Å resolution, Nature 411 (6840) (2001) 909.
[6] E.J. Boekema, A.F. Boonstra, J.P. Dekker, M. Rögner, Biomembranes, electron microscopic structural analysis of photosystem I, photosystem II, and the cytochromeb6/f complex from green plants and cyanobacteria, J.Bioenerg. 26 (1) (1994) 17–29.
[7] I. Sakurai, J.-R. Shen, J. Leng, S. Ohashi, M. Kobayashi, H. Wada, Lipids in oxygen-evolving photosystem II complexes of cyanobacteria and higher plants, J. Biochem. 140 (2) (2006) 201–209.
[8] J. Kern, A. Guskov, Lipids in photosystem II: multifunctional cofactors, J. Photochem. Photobiol. B Biol. 104 (1–2) (2011) 19–34.
[9] K. Gounaris, J. Barber, Monogalactosyldiacylglycerol: the most abundant polar lipid in nature, Trends Biochem. Sci. 8 (10) (1983) 378–381.
[10] C. Hunte, S. Richers, Lipids and membrane protein structures, Curr. Opin. Struct. Biol. 18 (4) (2008) 406–411.
[11] J.I. Ogren, A.L. Tong, S.C. Gordon, A. Chenu, Y. Lu, R.E. Blankenship, J. Cao, G. S. Schlau-Cohen, Impact of the lipid bilayer on energy transfer kinetics in the photosynthetic protein LH2, Chem. Sci. 9 (12) (2018) 3095–3104.
[12] T.H. Bayburt, Y.V. Grinkova, S.G. Sligar, Self-assembly of discoidal phospholipid bilayer nanoparticles with membrane scaffold proteins, Nano Lett. 2 (8) (2002) 853–856.
[13] G. Hazell, T. Arnold, R.D. Barker, L.A. Clifton, N.-J. Steinke, C. Tognoloni, K. J. Edler, Evidence of lipid exchange in styrene maleic acid lipid particle (SMALP) nanodisc systems, Langmuir 32 (45) (2016) 11845–11853.
[14] M. Overduin, M. Esmaili, Native nanodiscs and the convergence of lipidomics, metabolomics, interactomics and proteomics, Appl. Sci. 9 (6) (2019) 1230.
[15] L. Unger, A. Ronco-Campaña, P. Kitchen, R.M. Bill, A.J. Rothnie, Biological insights from SMA-extracted proteins, Biochem. Soc. Trans. 49 (3) (2021) 1349–1359.
[16] S. Scheidelaar, Martijn C. Koorengevel, Cornelius A. van Walree, Juan J. Dominguez, Jonas M. Dörr, J.A. Killian, Effect of polymer composition and pH

on membrane solubilization by styrene-maleic acid copolymers, Biophys. J. 111 (9) (2016) 1974–1986.
[17] N.G. Brady, C.E. Workman, B. Cawthon, B.D. Bruce, B.K. Long, Protein extraction efficiency and selectivity of esterified styrene-maleic acid copolymers in thylakoid membranes, Biomacromolecules 22 (6) (2021) 2544–2553.
[18] M. Golub, A. Kölsch, A. Feoktystov, A. Zouni, J. Pieper, Insights into solution structures of photosynthetic protein complexes from small-angle scattering methods, Crystals 11 (2) (2021) 203.
[19] N.G. Brady, S. Qian, B.D. Bruce, Analysis of styrene maleic acid alternating copolymer supramolecular assemblies in solution by small angle X-ray scattering, Eur. Polym. J. 111 (2019) 178–184.
[20] M.D. Phan, O.I. Korotych, N.G. Brady, M.M. Davis, S.K. Satija, J.F. Ankner, B. D. Bruce, X-ray and neutron reflectivity studies of styrene-maleic acid copolymer interactions with galactolipid-containing monolayers, Langmuir 36 (14) (2020) 3970–3980.
[21] D.A. Cherepanov, N.G. Brady, I.V. Shelaev, J. Nguyen, F.E. Gostev, M.D. Mamedov, V.A. Nadtochenko, B.D. Bruce, PSI-SMALP, a detergent-free cyanobacterial photosystem I, reveals faster femtosecond photochemistry, Biophys. J. 118 (2) (2020) 337–351.
[22] Z. Luo, D. Marson, Q.K. Ong, A. Loiudice, J. Kohlbrecher, A. Radulescu, A. Krause-Heuer, T. Darwish, S. Balog, R. Buonsanti, Quantitative 3D determination of self-assembled structures on nanoparticles using small angle neutron scattering, Nat. Commun. 9 (1) (2018) 1–10.
[23] M. Nakano, M. Fukuda, T. Kudo, H. Endo, T. Handa, Determination of interbilayer and transbilayer lipid transfers by time-resolved small-angle neutron scattering, Phys. Rev. Lett. 98 (23) (2007), 238101.
[24] S.R. Midtgaard, T.A. Darwish, M.C. Pedersen, P. Huda, A.H. Larsen, G.V. Jensen, S. A.R. Kynde, N. Skar-Gislinge, A.J.Z. Nielsen, C. Olesen, Invisible detergents for structure determination of membrane proteins by small-angle neutron scattering, FEBS J. 285 (2) (2018) 357–371.
[25] M. Jamshad, V. Grimard, I. Idini, T.J. Knowles, M.R. Dowle, N. Schofield, P. Sridhar, Y. Lin, R. Finka, M. Wheatley, Structural analysis of a nanoparticle containing a lipid bilayer used for detergent-free extraction of membrane proteins, Nano Res. 8 (3) (2015) 774–789.
[26] P.A. Timmins, M. Leonhard, H.U. Weltzien, T. Wacker, W. Welte, A physical characterization of some detergents of potential use for membrane protein crystallization, FEBS Lett. 238 (2) (1988) 361–368.
[27] R.K. Le, B.J. Harris, I.J. Iwuchukwu, B.D. Bruce, X. Cheng, S. Qian, W.T. Heller, H. O'Neill, P.D. Frymier, Analysis of the solution structure of thermosynechococcus elongatus photosystem I in n-dodecyl-beta-D-maltoside using small-angle neutron scattering and molecular dynamics simulation, Arch. Biochem. Biophys. 550–551 (2014) 50–57.
[28] T. Iwamura, H. Nagai, S.-E. Ichimura, Improved methods for determining contents of chlorophyll, protein, ribonucleic acid, and deoxyribonucleic acid in planktonic populations, Int.Rev.gesamten Hydrobiol.Hydrogr. 55 (1) (1970) 131–147.
[29] W.T. Heller, M. Cuneo, L. Debeer-Schmitt, C. Do, L. He, L. Heroux, K. Littrell, S. V. Pingali, S. Qian, C. Stanley, The suite of small-angle neutron scattering instruments at Oak Ridge National Laboratory, J. Appl. Crystallogr. 51 (2) (2018) 242–248.
[30] P.V. Konarev, V.V. Volkov, A.V. Sokolova, M.H. Koch, D.I. Svergun, PRIMUS: a windows PC-based system for small-angle scattering data analysis, J. Appl. Crystallogr. 36 (5) (2003) 1277–1282.
[31] D. Svergun, Determination of the regularization parameter in indirect-transform methods using perceptual criteria, J. Appl. Crystallogr. 25 (4) (1992) 495–503.
[32] P. Joliot, A. Joliot, In vivo analysis of the electron transfer within photosystem I: are the two phylloquinones involved? Biochemistry 38 (34) (1999) 11130–11136.
[33] S. Xiao, W. Gao, Q.-F. Chen, S.-W. Chan, S.-X. Zheng, J. Ma, M. Wang, R. Welti, M.-L. Chye, Overexpression of Arabidopsis acyl-CoA binding protein ACBP3 promotes starvation-induced and age-dependent leaf senescence, Plant Cell 22 (5) (2010) 1463–1482.
[34] D.J. Swainsbury, S. Scheidelaar, R. van Grondelle, J.A. Killian, M.R. Jones, Bacterial reaction centers purified with styrene maleic acid copolymer retain native membrane functional properties and display enhanced stability, Angew. Chem. Int. Ed. Engl. 53 (44) (2014) 11803–11807.
[35] M. Jamshad, Y.P. Lin, T.J. Knowles, R.A. Parslow, C. Harris, M. Wheatley, D. R. Poyner, R.M. Bill, O.R. Thomas, M. Overduin, T.R. Dafforn, Surfactant-free purification of membrane proteins with intact native membrane environment, Biochem. Soc. Trans. 39 (3) (2011) 813–818.
[36] T.J. Knowles, R. Finka, C. Smith, Y.-P. Lin, T. Dafforn, M. Overduin, Membrane proteins solubilized intact in lipid containing nanoparticles bounded by styrene maleic acid copolymer, J. Am. Chem. Soc. 131 (22) (2009) 7484–7485.
[37] K. Kobayashi, K. Endo, H. Wada, Specific distribution of phosphatidylglycerol to photosystem complexes in the thylakoid membrane, FrontiersPlant Sci. 8 (2017).
[38] O. Korotych, J. Mondal, K.M. Gattás-Asfura, J. Hendricks, B.D. Bruce, Evaluation of commercially available styrene-co-maleic acid polymers for the extraction of membrane proteins from spinach chloroplast thylakoids, Eur. Polym. J. 114 (2019) 485–500.
[39] E. El-Mohsnawy, M.J. Kopczak, E. Schlodder, M. Nowaczyk, H.E. Meyer, B. Warscheid, N.V. Karapetyan, M. Rögner, Structure and function of intact photosystem 1 monomers from the Cyanobacterium Thermosynechococcus elongatus, Biochemistry 49 (23) (2010) 4740–4751.
[40] M. Hippler, F. Drepper, J.-D. Rochaix, U. Mühlenhoff, Insertion of the N-terminal part of PsaF from Chlamydomonas reinhardtii into photosystem I from Synechococcus elongatus enables efficient binding of algal plastocyanin and cytochrome c 6, J. Biol. Chem. 274 (7) (1999) 4180–4188.
[41] K. Endo, K. Kobayashi, H. Wada, Sulfoquinovosyldiacylglycerol has an essential role in Thermosynechococcus elongatus BP-1 under phosphate-deficient conditions, Plant Cell Physiol. 57 (12) (2016) 2461–2471.
[42] F.J. van Eerden, D.H. de Jong, A.H. de Vries, T.A. Wassenaar, S.J. Marrink, Characterization of thylakoid lipid membranes from cyanobacteria and higher plants by molecular dynamics simulations, Biochim. Biophys. Acta Biomembr. 1848 (6) (2015) 1319–1330.
[43] C. MacGregor-Chatwin, M. Sener, S.F.H. Barnett, A. Hitchcock, M.C. Barnhart-Dailey, K. Maghlaoui, J. Barber, J.A. Timlin, K. Schulten, C.N. Hunter, Lateral segregation of photosystem I in cyanobacterial thylakoids, Plant Cell 29 (5) (2017) 1119–1136.
[44] D.J. Swainsbury, M.S. Proctor, A. Hitchcock, M.L. Cartron, P. Qian, E.C. Martin, P. J. Jackson, J. Madsen, S.P. Armes, C.N. Hunter, Probing the local lipid environment of the Rhodobacter sphaeroides cytochrome bc1 and Synechocystis sp. PCC 6803 cytochrome b6f complexes with styrene maleic acid, Biochim. Biophys. Acta Bioenerg. 1859 (3) (2018) 215–225.